

Structure–Transport Correlation Reveals Anisotropic Charge Transport in Coupled PbS Nanocrystal Superlattices

Andre Maier, Dmitry Lapkin, Nastasia Mukharamova, Philipp Frech, Dameli Assalauova, Alexandr Ignatenko, Ruslan Khubbutdinov, Sergey Lazarev, Michael Sprung, Florian Laible, Ronny Löffler, Nicolas Previdi, Annika Bräuer, Thomas Günkel, Monika Fleischer, Frank Schreiber, Ivan A. Vartanyants,* and Marcus Scheele*

The assembly of colloidal semiconductive nanocrystals into highly ordered superlattices predicts novel structure-related properties by design. However, those structure–property relationships, such as charge transport depending on the structure or even directions of the superlattice, have remained unrevealed so far. Here, electric transport measurements and X-ray nanodiffraction are performed on self-assembled lead sulfide nanocrystal superlattices to investigate direction-dependent charge carrier transport in microscopic domains of these materials. By angular X-ray cross-correlation analysis, the structure and orientation of individual superlattices is determined, which are directly correlated with the electronic properties of the same microdomains. By that, strong evidence for the effect of superlattice crystallinity on the electric conductivity is found. Further, anisotropic charge transport in highly ordered monocrystalline domains is revealed, which is attributed to the dominant effect of shortest interparticle distance. This implies that transport anisotropy should be a general feature of weakly coupled nanocrystal superlattices.

Semiconductive nanocrystals (NCs) can be self-assembled into ordered superlattices (SLs) to create artificial solids with emerging collective properties.^[1–3] Computational studies have predicted that properties such as electronic coupling or charge transport are determined not only by the individual NCs but also by the degree of their organization and structure.^[4–7] However, experimental proof for a correlation between structure

and charge transport in NC SLs is still pending. Previous experimental research on NC SLs has either focused solely on the process of self-organization and structural order^[8–13] or, in separate studies, on charge transport, and electronic properties.^[14–19] In order to reveal potential transport anisotropy, a correlated investigation of charge transport and structural order on the same NC SL is required. This allows addressing a variety of fundamental questions. Are the electronic properties of NC SLs influenced by the SL type and orientation? Do polycrystalline and monocrystalline SLs differ in conductivity? What is the degree of transport anisotropy in NC SLs?

Here, we address these questions by a direct correlation of the structural and electronic properties of SLs composed of electronically coupled lead sulfide (PbS)

NCs. We perform X-ray nanodiffraction and apply angular X-ray cross-correlation analysis (AXCCA)^[8,20,21] to characterize the structure of the SLs, which are correlated with electric transport measurements of the same microdomains. By that, we reveal anisotropic charge transport in highly ordered monocrystalline hexagonal-close-packed (hcp) PbS NC SLs and find strong evidence for the effect of SL crystallinity on charge transport.

A. Maier, P. Frech, N. Previdi, Dr. M. Scheele
Institute of Physical and Theoretical Chemistry
University of Tuebingen
Auf der Morgenstelle 18, Tuebingen 72076, Germany
E-mail: marcus.scheele@uni-tuebingen.de

A. Maier, Dr. F. Laible, Dr. R. Löffler, A. Bräuer, Prof. M. Fleischer,
Prof. F. Schreiber, Dr. M. Scheele
Center for Light-Matter Interaction, Sensors & Analytics LISA+
University of Tuebingen
Auf der Morgenstelle 15, Tuebingen 72076, Germany

 The ORCID identification number(s) for the author(s) of this article can be found under <https://doi.org/10.1002/adma.202002254>.

© 2020 The Authors. Published by WILEY-VCH Verlag GmbH & Co. KGaA, Weinheim. This is an open access article under the terms of the Creative Commons Attribution-NonCommercial License, which permits use, distribution and reproduction in any medium, provided the original work is properly cited and is not used for commercial purposes.

DOI: 10.1002/adma.202002254

D. Lapkin, N. Mukharamova, D. Assalauova, Dr. A. Ignatenko,
R. Khubbutdinov, Dr. S. Lazarev, Dr. M. Sprung, Prof. I. A. Vartanyants
Deutsches Elektronen-Synchrotron DESY
Notkestraße 85, Hamburg 22607, Germany
E-mail: ivan.vartanyants@desy.de

R. Khubbutdinov, Prof. I. A. Vartanyants
National Research Nuclear University MEPhI
(Moscow Engineering Physics Institute)
Kashirskoe shosse 31, Moscow 115409, Russia

Dr. F. Laible, A. Bräuer, T. Günkel, Prof. M. Fleischer, Prof. F. Schreiber
Institute of Applied Physics
University of Tuebingen
Auf der Morgenstelle 10, Tuebingen 72076, Germany

Dr. S. Lazarev
National Research Tomsk Polytechnic University (TPU)
pr. Lenina 30, Tomsk 634050, Russia

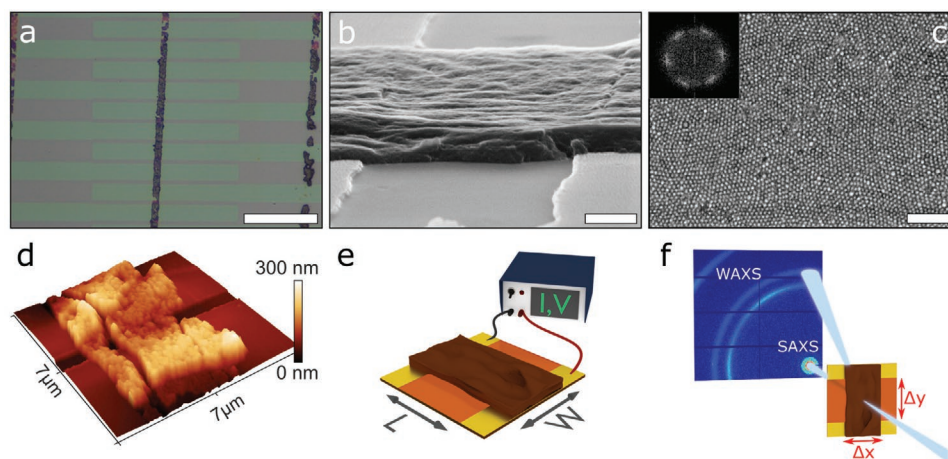


Figure 1. Microchannels of PbS NC SLs for conductivity and X-ray nanodiffraction measurements. a) Optical microscopy image of an orthogonal PbS NC stripe connecting adjacent electrodes to form individually addressable microchannels. Scale bar: 40 μm . b) SEM image in sideview (85° from normal) of a typical microchannel consisting of a ≈ 200 nm thick PbS NC SL stripe across two Au electrodes. Scale bar: 300 nm. c) High-resolution SEM image showing self-assembled PbS NCs within a microchannel with near-range order, as indicated by the fast Fourier transform (inset). Scale bar: 100 nm. d) AFM image of a microchannel on a Kapton substrate. e, f) Schematics of a SL domain on a Kapton device forming a microchannel with length $L \approx 1$ μm and width $W \approx 4$ μm to characterize the electronic properties (e) as well as the structural properties with X-ray nanodiffraction by means of SAXS and WAXS (f). Spatial mapping is performed along Δx and Δy directions.

As a model system we use oleic acid (OA) capped PbS NCs with a diameter of 5.8 ± 0.5 nm, which are self-assembled and functionalized with the organic π -system Cu-4,4',4'',4'''-tetraaminophthalocyanine (Cu4APc) at the liquid–air interface (details in Figures S1 and S2, Supporting Information).^[22] This results in long-range ordered and highly conductive SLs, since the rigid and relatively long ligands reduce the energy barrier for charge transport without deteriorating structural order, as it was shown previously.^[23,24] Hence, the hybrid system of PbS NCs and Cu4APc is an ideal compromise between increased electronic coupling and long-range ordered SLs, which was a fundamental prerequisite for this study. By means of soft-lithographic micro-contact printing,^[25] we transfer stripes of PbS NC-Cu4APc SLs with a width (W) of roughly 4 μm onto trenches of ≈ 1 μm length (L) between two gold contacts on X-ray transparent Kapton and Si/SiO_x substrates. This defines individually addressable microchannels with $L \approx 1$ μm , $W \approx 4$ μm , and thickness h (Figure 1a–e). Since this area is comparable to the typical grain size of PbS NC SLs,^[21] these microchannels enable transport measurements in single-crystalline PbS SLs.

In Figure 2, we display the charge transport characteristics of the microchannels as well as its dependence on the thickness of the SL and the probed area. The conductivity σ is calculated as $\sigma = (G \cdot L)/(W \cdot h)$ for all individual microchannels from two-point probe conductance (G) measurements (Figures 1e and 2a). Within the approximately two hundred individual microchannels measured, we observe electric conductivities in a wide range of values (10^{-6} – 10^{-3} S m⁻¹) (Figure 2b). This distribution correlates with the thickness of the SL (Figure 2c), which also varies by two orders of magnitude over the large number of microchannels analyzed here. The correlation is non-linear with a maximum in σ for thicknesses from 70 nm to 200 nm. Using Si/SiO_x as substrate, we performed field-effect transistor measurements of the PbS NC-Cu4APc SLs, revealing p-type behavior, which agrees with our previous study (Figure S3,

Supporting Information).^[23] The microchannels show hole-mobilities up to $\mu \approx 10^{-4}$ cm² V⁻¹ s⁻¹. Based on these transport properties and previous reports on the importance of mid-gap states in PbS NC materials, we believe that transport in the present material occurs predominantly via hopping through trap states close to the valence eigenstate (the 1S_h state).^[5,26,27]

We tested the effect of domain boundaries within the SL on electric transport on the same substrates measuring the geometry-normalized conductance of PbS NC SLs over large active channel areas of $\approx 10^4$ μm^2 (Figure S4, Supporting Information). As shown in Figure 2d, electric transport in this case is approximately two orders of magnitude less efficient than within the microchannels of ≈ 4 μm^2 , indicating the advantageous effect of the near single-crystalline channels present in the latter case (see below).

Further investigations of structural properties of the same microchannels on Kapton substrates using X-ray nanodiffraction in correlation with conductivity measurements are the focus of this study (Figure 1e,f, Figure S5, Supporting Information). We determined the structural details of all microchannels by X-ray nanodiffraction (Experimental Section and Figures S6–S9, Supporting Information). Using a nanofocused X-ray beam, we collected diffraction patterns at different positions in each channel (Figure 1f). Two typical small-angle X-ray scattering (SAXS) and wide-angle X-ray scattering (WAXS) diffraction patterns from representative microchannels, averaged over all positions within these channels, are shown in Figure 3a,g,b,h. For some of the microchannels we observe several orders of Bragg peaks in SAXS attributed to monocrystalline SLs (Figure 3a), whereas the rest of the channels demonstrate continuous Debye–Scherrer rings with low intensity modulations corresponding to polycrystalline SLs (Figure 3g). From the angular-averaged profiles, shown in Figure 3c,i, we revealed two dominant SL structures: a monocrystalline, random hexagonal-close-packed (rhcp) lattice mainly oriented along the $[0001]_{\text{SL}}$, and a polycrystalline,

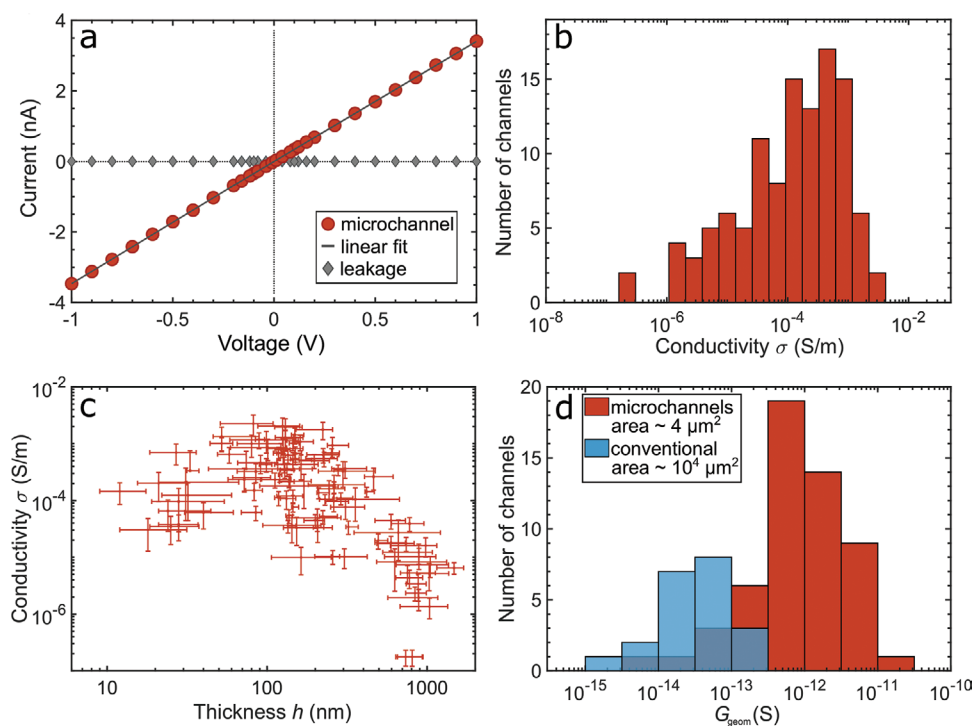


Figure 2. Electrical transport measurements of SL microchannels. a) Typical I - V curve of a PbS NC SL within a microchannel showing Ohmic behavior (red). The leak current through the dielectric substrate is negligible (gray). b) Distribution of the electric conductivities of 200 individual microchannels. c) Conductivity of the microchannels as a function of PbS NC SL thickness. The error bars represent the standard deviation of conductivity and the range of thickness determined by AFM, respectively. d) Distribution of geometry-normalized conductance of conventional large area and microchannels, probing effective areas of $\approx 10^4 \mu\text{m}^2$ (blue) and $\approx 4 \mu\text{m}^2$ (red), respectively. Measured conductance values are normalized to the channel geometry (L/W). The dark blue color corresponds to the overlap of the distributions.

body-centered-cubic (bcc) lattice primarily oriented along the $[110]_{\text{SL}}$ (scanning electron microscopy (SEM) images given in Figure S13, Supporting Information). From the peak positions in SAXS, we estimated the unit cell parameters (a_{rhcp} and a_{bcc}) for each channel and corresponding nearest-neighbor distances (NNDs), which are $d_{\text{NN}} = a_{\text{rhcp}}$ for rhcp and $d_{\text{NN}} = (\sqrt{3}/2) \cdot a_{\text{bcc}}$ for bcc, respectively. The averaged NNDs for all rhcp and bcc channels are $7.8 \pm 0.4 \text{ nm}$ and $6.9 \pm 0.2 \text{ nm}$, respectively. In WAXS (Figure 3b,h), we observe parts of three Debye-Scherrer rings corresponding to $\{111\}_{\text{AL}}$, $\{200\}_{\text{AL}}$, $\{220\}_{\text{AL}}$ reflections of the PbS atomic lattice (AL). From the single WAXS pattern analysis we found different degrees of angular disorder of NCs: roughly 24° for rhcp and 16° for bcc channels (Figure S9, Supporting Information).

To study the relative orientation of the NCs inside the SL, we applied AXCCA,^[20] which is based on the analysis of the cross-correlation functions (CCFs), to the measured scattering data (Figures S10–S12, Supporting Information). We evaluated the CCFs for the SL and AL peaks for both rhcp and bcc structures. We found that in the rhcp monocrystalline channels (Figure 3d) the $[111]_{\text{AL}}$ and $[110]_{\text{AL}}$ directions of the NCs are collinear to the $[0001]_{\text{SL}}$ and $[2\bar{1}\bar{1}0]_{\text{SL}}$ directions, respectively (Figure 3f). In bcc polycrystalline channels (Figure 3j), all corresponding SL and AL directions are aligned (e.g., $\langle 100 \rangle_{\text{SL}}$ and $\langle 100 \rangle_{\text{AL}}$), as shown in Figure 3l. The similarity between the experimental CCFs and simulated CCFs for these structures confirms the obtained angular orientation of the NCs in the SL (Figure 3d,e and Figure 3j,k, respectively).

Upon correlating the X-ray with the electric transport measurements, we found that microchannels containing the polycrystalline bcc SLs exhibit higher conductivity than monocrystalline rhcp SLs over the entire range of thicknesses (Figure 4a). This can in part be understood in terms of the shorter NND which exponentially increases the hopping probability (Figure 4b).^[4,15] The microchannels exhibit strong characteristic Raman signals for Cu4APc (750 cm^{-1} and $1050\text{--}1650 \text{ cm}^{-1}$, Figure 4c,d), which vanish for probing areas outside the microchannels, verifying the specific functionalization of the NCs with the organic π -system (Figure S14, Supporting Information). We used the intensity of the two characteristic Raman bands to compare the relative density of Cu4APc molecules within different SLs. We found that polycrystalline bcc SLs with the smaller NND exhibit generally stronger Raman signals from Cu4APc than monocrystalline rhcp SLs with larger NND (Figure 4c,d and Figure S14, Supporting Information). This means that in monocrystalline rhcp SLs fewer native OA molecules have been exchanged by Cu4APc, resulting in larger interparticle distances, which adversely affects conductivity. From Figure 4b one can identify several cases of monocrystalline rhcp SLs having conductivities as high as those of polycrystalline bcc SLs ($\sigma \approx 10^{-4}\text{--}10^{-3} \text{ S m}^{-1}$), although the NND is much larger. We consider this as supporting evidence that the degree of SL crystallinity (poly versus mono) has a significant effect on the conductivity, which, in the present example, compensates the effect of the much larger interparticle distance. The SLs with

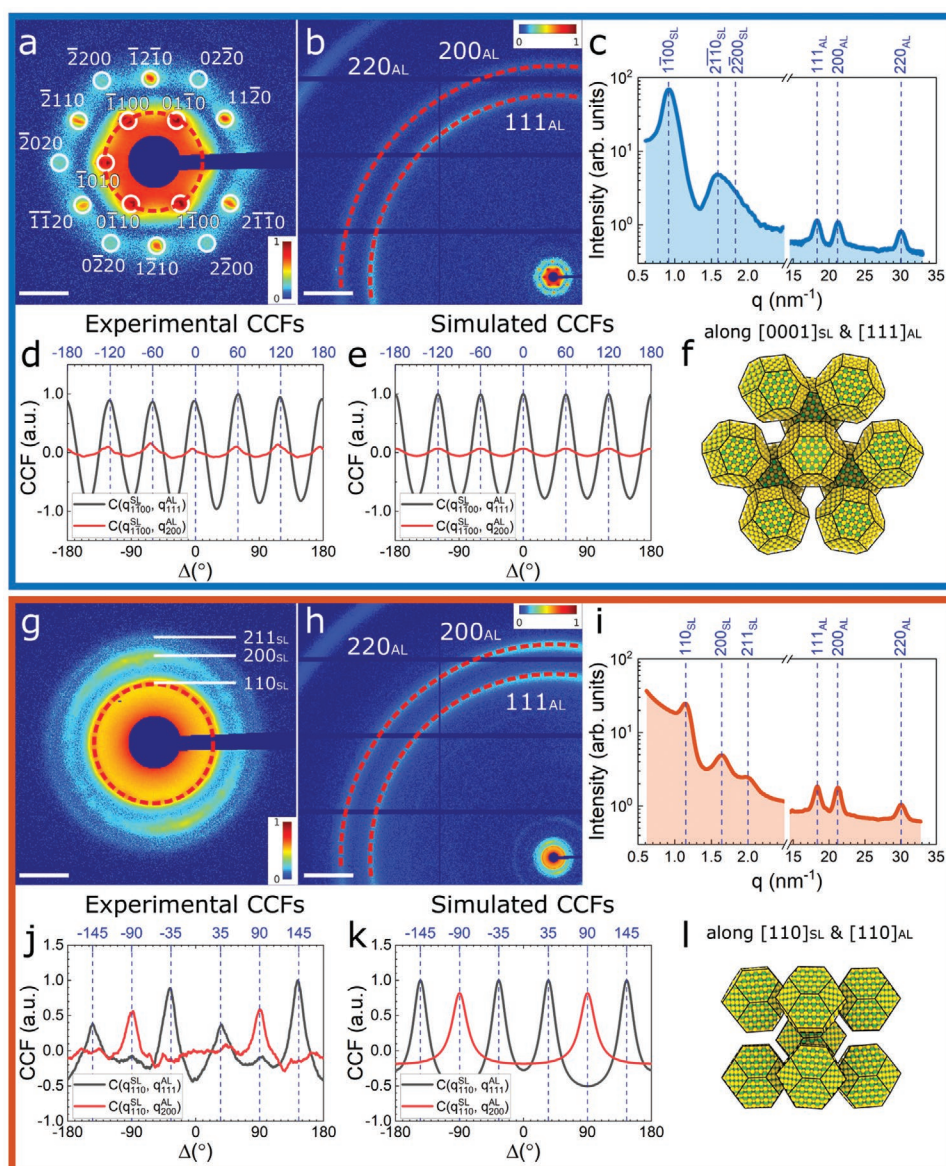


Figure 3. Structural investigation of the SL structures. a,b,g,h) Exemplary SAXS (a,g) and WAXS (b,h) patterns averaged over one microchannel for two typical cases: a,b) a monocrystalline rhcp SL oriented along $[0001]_{\text{SL}}$ and g,h) a polycrystalline bcc SL oriented along $[110]_{\text{SL}}$. c,i) Azimuthally averaged intensity profiles of SAXS ($q < 2.5 \text{ nm}^{-1}$) and WAXS ($q > 15 \text{ nm}^{-1}$) signals of the two SL types. d,j) Averaged CCFs for the two SL types, calculated for the first SAXS peaks ($\langle 1\bar{1}00 \rangle_{\text{SL}}$ in the rhcp case (d) and $\langle 110 \rangle_{\text{SL}}$ in the bcc case (j)) and the $\langle 111 \rangle_{\text{AL}}$ or $\langle 200 \rangle_{\text{AL}}$ WAXS peaks. e,k) Simulated CCFs for the two models shown in (f,l). f,l) Schematic drawing of the proposed SL structures: f) $[0001]_{\text{SL}}$ -oriented rhcp SL of PbS NCs, where the NCs are aligned as indicated and l) $[110]_{\text{SL}}$ -oriented bcc SL of PbS NCs, where all the corresponding SL and AL directions are aligned. For clarity, ligand spheres are omitted. Scale bars in (a,g) and (b,h) correspond to 1 nm^{-1} and 5 nm^{-1} , respectively.

smaller interparticle distance exhibit stronger Raman signals from Cu4APc compared to larger SLs (Figure S14, Supporting Information), corroborating a correlation between interparticle distance and ligand exchange. In fact, the smallest lattice parameter of $\approx 6.8 \text{ nm}$ in Figure 4b corresponds to an interparticle distance of $\approx 1 \text{ nm}$, which is approximately the length of one Cu4APc molecule or the minimal width of a fully exchanged ligand sphere. In contrast, residual OA leads to greater interparticle distances due to steric interactions of adjacent OA shells,^[28] explaining the spread of the NNDs (Figure 4b and Figure S8, Supporting Information). The occurrence of the

two SL types (rhcp and bcc) found here may be related to the previously observed hcp–bcc transition for OA-capped PbS NC SLs upon tailored solvent evaporation.^[29] Similarly, our polycrystalline bcc SLs are assembled from PbS NCs dispersed in hexane, whereas hexane-octane mixtures resulted in monocrystalline rhcp SLs. This invokes different solvent evaporation rates, which may lead to distinct SL unit cells.^[13,28]

From the single WAXS pattern analysis (Figure S9, Supporting Information) we found that NCs are aligned in the superlattice with different degrees of angular disorder: roughly 16° for bcc channels and 24° for rhcp channels. We believe that the NCs

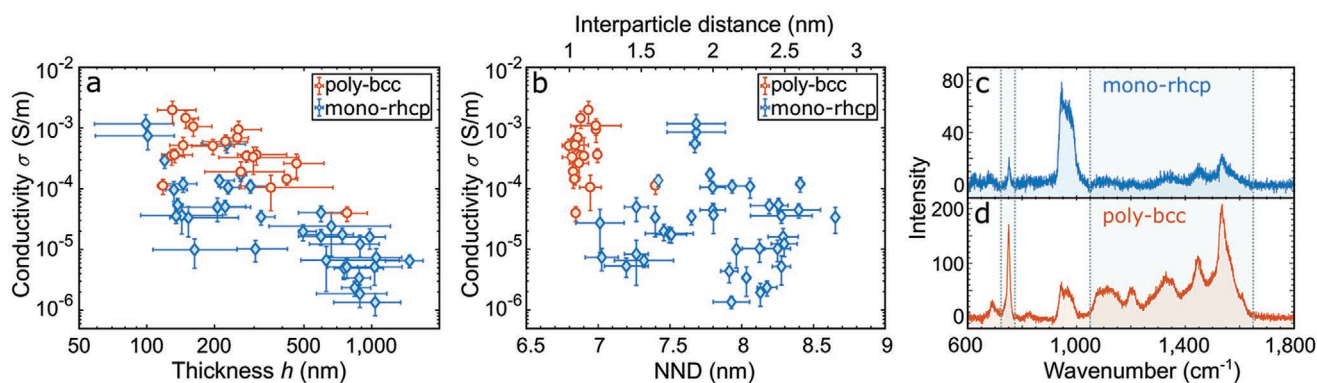


Figure 4. Parameters for structure–transport correlations. a,b) Conductivity of individual microchannels as a function of SL thickness (a) and NND (b). The SL type is indicated by the color code. c,d) Typical Raman spectra of a monocrystalline rhcp (c) and a polycrystalline bcc (d) SL, featuring characteristic Cu4APc signals at 750 cm^{-1} and $1050\text{--}1650\text{ cm}^{-1}$ (highlighted regions). The signal at $\approx 950\text{ cm}^{-1}$ originates from the Si/SiO_x substrate.

are oriented in the superlattice due to facet-specific ligand–ligand interactions. The functionalization of NCs with shorter Cu4APc ligands leads to the formation of a superlattice with higher symmetry, such as bcc, in which the NCs are highly aligned.^[30] In contrast, a large spherical ligand shell leads to a close-packed structure with a lower degree of NCs orientation, such as rhcp.

In view of the non-monotonic correlation between conductivity and SL thickness, we note that very thin NC films exhibit holes/microcracks, which are reduced with increasing thickness.^[31] In contrast, the conductivity in thick films may be affected by a fringing electric field. The electric field is not homogeneous along the sample normal, and current flows mainly in the bottom

layers close to the contacts. However, the conductivity is calculated over the entire channel where the full height is used.

We now turn to the key novelty of this work, the transport anisotropy, that is, the influence of the SL orientation with respect to the electric field on the electric conductivity. For this, it is mandatory to account for the effect of SL thickness, incomplete ligand exchange and crystallinity, and only compare SLs which are very similar in this regard. In doing so, we found strong evidence for a favored angular direction of charge carrier hopping, indicating anisotropic charge transport within the SL. **Figure 5a,d** displays exemplary SAXS patterns averaged over each microchannel of two monocrystalline rhcp SLs with identical

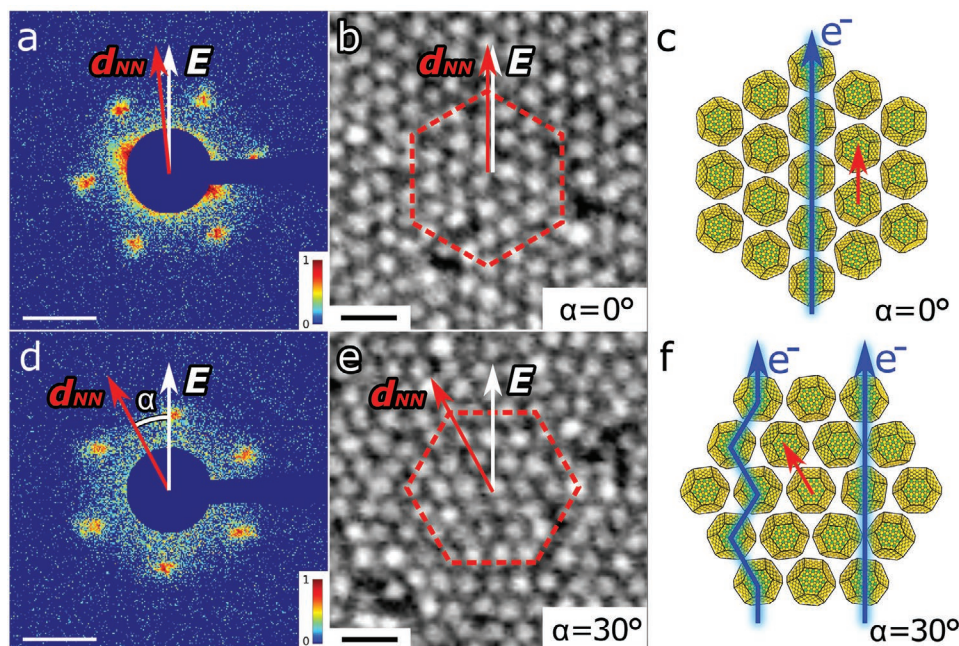


Figure 5. Anisotropic charge transport in monocrystalline NC SLs. a,d) Exemplary averaged SAXS diffraction patterns of comparable monocrystalline rhcp microchannels, oriented along $[0001]_{\text{SL}}$. The azimuthal orientation is defined by the relative angle α between the electric field vector E and the nearest-neighbor direction d_{NN} . SLs with low values of α feature 40–50% higher conductivities than their counterparts with large α . Scale bar: 1 nm^{-1} . b,e) Corresponding real-space SEM images of the SL oriented along $(0001)_{\text{SL}}$ with $\alpha = 0^\circ$ and 30° . The hexagon indicates the orientation of the SL. d_{NN} points along the alignment of the NCs (nearest neighbors). For $\alpha = 0^\circ$, the vector d_{NN} is parallel to E , resulting in enhanced conductivity. Scale bar: 15 nm . c,f) Schematic of the rhcp SL and the favored hopping path for $\alpha = 0^\circ$ (blue arrow) along the d_{NN} direction (red arrow) (c); for an in-plane offset ($\alpha = 30^\circ$), the larger hopping distance or the zig-zag path are detrimental to charge transport (f). Ligand spheres of NCs are omitted for clarity.

structure, that is, lattice parameter and thickness (Figure S15a, Supporting Information). They differ only in terms of the azimuthal orientation with respect to the applied electric field. We define the azimuthal angle α between the electric field vector E (which is oriented vertically due to horizontal electrode edges) and the nearest-neighbor direction d_{NN} (one of the $\langle 2110 \rangle_{\text{SL}}$ directions pointing to the nearest-neighbors). The angle α can vary from 0° to 30° for the sixfold in-plane symmetry. For $\alpha = 0^\circ$, the d_{NN} direction is oriented parallel to the vector of electric field E , whereas for $\alpha = 30^\circ$, the angular (in-plane) offset between the vectors E and d_{NN} is maximized. Our key result is that for any two otherwise comparable channels, we observe higher conductivity for the respective channels with lower angle α . The two extremes ($\alpha = 0^\circ$ and $\alpha = 30^\circ$) are shown in the corresponding real-space SEM images of the $(0001)_{\text{SL}}$ plane of two rhcp SLs in Figure 5b,e. The difference in conductivity between two otherwise identical SLs is 40–50%. A statistical investigation of other microchannels with monocrystalline rhcp SLs reveals similar α -dependent conductivity differences (Figure S15, Supporting Information). This correlation between σ and α indicates anisotropic charge transport, for which the direction of nearest neighbors is assumed to be the most efficient for transport.

In contrast to atomic crystals with transport anisotropy, which exhibit strong electronic coupling and ballistic transport (e.g., black phosphorus), the NC SLs studied here are in the weak coupling regime. This implies temperature-activated hopping as the predominant charge transport mechanism and invokes a strong dependence on the hopping distance.^[4,15] Our results suggest that charge transport is most efficient if the applied electric field is iso-oriented with the nearest-neighbor direction d_{NN} in the SL plane, since this leads to the shortest hopping distance (Figure 5c). Any other orientation (Figure 5f) results either in a larger hopping distance (straight arrow) or a deviation from the direction of the electric field together with an increased number of required jumps for electrons to travel the same distance (zig-zag path), which is detrimental to charge transport. This implies that transport anisotropy should be a general feature of weakly coupled, monocrystalline NC SLs, originating from the dominant effect of the shortest interparticle distance. Accordingly, one could predict the favored direction of charge transport within different SL types, such as simple cubic, face-centered cubic (fcc), or bcc, being the $\langle 100 \rangle$, $\langle 110 \rangle$, or $\langle 111 \rangle$ SL directions, respectively. A similar charge transport anisotropy was computationally predicted for bcc and fcc SLs.^[6] Further, we note that the orientational order of the NCs observed here might be an additional source for anisotropic charge transport as different coupling strengths have been predicted along particular AL directions.^[5,6] In the present case, the most efficient transport occurs if the $[110]_{\text{AL}}$ direction of all NCs is iso-oriented with the electric field.

A high degree of control provided over the SL type and orientation would enable the exploitation of such transport anisotropy also with more complex NC assemblies (e.g., binary NC SLs^[32] or honeycomb structures^[33]) for application in functional electronic devices with tailored transport anisotropy. Furthermore, these results constitute an important step toward the understanding of the intrinsic properties and fundamental limits of these fascinating new NC-based systems.

Experimental Section

Superlattice Microchannel Fabrication: Oleic-acid-stabilized PbS NCs were synthesized according to Weidman et al.^[34] and dispersed in hexane/octane (ratio of 4:1 and 1:0, $c = 4 \mu\text{mol L}^{-1}$). Sizing-curves to UV-vis absorption spectra and SEM investigation yield a particle size of $5.8 \pm 0.5 \text{ nm}$ (Figure S1, Supporting Information).^[35] The NCs were self-assembled at the liquid-air interface according to Dong et al.^[22] and ligand exchanged with the organic π -system Cu-4,4',4'',4'''-tetraaminophthalocyanine. For microcontact printing, a micropatterned PDMS stamp was inked with the SL film and stamped onto devices with pre-patterned Au electrodes (Kapton membranes of $125 \mu\text{m}$ thickness or Si/SiO₂ wafer with 200 nm SiO_2). Individual microchannels consisting of an electrode pair and a connecting SL stripe were obtained with $L \approx 1 \mu\text{m}$ and $W \approx 4 \mu\text{m}$. The preparation was performed in a nitrogen glovebox.

Transport Measurements: All devices were measured at room temperature in a nitrogen flushed probe station (Lake Shore, CRX-6.5K). Individual electrode pairs were contacted and analyzed by a source-meter-unit (Keithley, 2636B).

X-Ray Nanodiffraction: Nanodiffraction measurements were performed at Coherence beamline P10 of the PETRA III synchrotron source at DESY. An X-ray beam with $\lambda = 0.898 \text{ nm}$ ($E = 13.8 \text{ keV}$) was focused down to a spot size of $\approx 400 \times 400 \text{ nm}^2$ (FWHM) at the GINIX nanodiffraction endstation.^[36] The 2D detector EIGER X4M (Dectris) with 2070×2167 pixels and a pixel size of $75 \times 75 \mu\text{m}^2$ was positioned 370 mm downstream from the sample and $\approx 9 \text{ cm}$ off-center to allow simultaneous detection of SAXS and WAXS signals. Diffraction mapping of individual microchannels was performed, collecting 100–200 diffraction patterns on a raster grid in Δx and Δy direction with 250 nm step size and an acquisition of 0.5 s . From averaged diffraction patterns for every channel, the SL structure was deduced and from azimuthally-averaged radial profiles the SAXS peak positions were extracted. AXCCA was applied and two-point cross-correlation functions (CCFs) for all channels were calculated, according to Equation (1)

$$C(q_{\text{SL}}, q_{\text{AL}}, \Delta) = \langle \tilde{I}(q_{\text{SL}}, \varphi) \tilde{I}(q_{\text{AL}}, \varphi + \Delta) \rangle_{\varphi} \quad (1)$$

where $\tilde{I}(q_{\text{SL}}, \varphi) = I(q_{\text{SL}}, \varphi) - \langle I(q_{\text{SL}}, \varphi) \rangle_{\varphi}$ and $I(q_{\text{SL}}, \varphi)$ is an intensity value taken at the point (q_{SL}, φ) which are polar coordinates in the detector plane.^[8,20,21] $\langle \dots \rangle_{\varphi}$ denotes averaging over all azimuthal φ angles. q_{SL} correspond to SAXS peaks and q_{AL} to WAXS peaks.

Microchannel Characterization: SEM imaging was conducted with a HITACHI model SU8030 at 30 kV and atomic force microscopy (AFM) investigations with a Bruker MultiMode 8-HR in contact mode and Raman spectroscopy with a confocal Raman spectrometer LabRAM HR800 (Horiba Jobin-Yvon) at $\lambda = 632.8 \text{ nm}$ (He-Ne-laser).

Details on materials, the self-assembly and fabrication processes, X-ray nanodiffraction and AXCCA are given in the Supporting Information.

Supporting Information

Supporting Information is available from the Wiley Online Library or from the author.

Acknowledgements

This project has been funded by the DFG under Grant SCHE1905/3-2 and INST 37/829-1 FUGG, the latter for SEM measurements using a Hitachi SU 8030. Further funding was provided by the Helmholtz Associations Initiative Networking Fund and the Russian Science Foundation grant HRSF-0002/18-41-06001, and the Tomsk Polytechnic University Competitiveness Enhancement Program grant (project number VIU-MNOL NK-214/2018). The authors acknowledge support and discussions with E. Weckert. T. Salditt's group is acknowledged for providing nanofocusing instrument (GINIX) support at the P10 beamline. The

construction and operation of the GINIX setup is funded by the Georg-August Universität Göttingen and BMBF Verbundforschung "Struktur der Materie", projects 05KS7MGA, 05K10MGA, and 05K13MG4.

Conflict of Interest

The authors declare no conflict of interest.

Keywords

charge transport, nanocrystals, nanodiffraction, self-assembly, superlattices

Received: April 1, 2020

Revised: June 17, 2020

Published online: July 28, 2020

-
- [1] C. B. Murray, C. R. Kagan, M. G. Bawendi, *Science* **1995**, 270, 1335.
 [2] A. P. Alivisatos, *Science* **1996**, 271, 933.
 [3] C. R. Kagan, C. B. Murray, *Nat. Nanotechnol.* **2015**, 10, 1013.
 [4] F. Remacle, R. D. Levine, *ChemPhysChem* **2001**, 2, 20.
 [5] N. Yazdani, S. Andermatt, M. Yarema, V. Farto, M. H. Bani-Hashemian, S. Volk, W. M. M. Lin, O. Yarema, M. Luisier, V. Wood, *Nat. Commun.* **2020**, 11, 2852.
 [6] A. P. Kaushik, B. Lukose, P. Clancy, *ACS Nano* **2014**, 8, 2302.
 [7] P. Liljeroth, K. Overgaard, A. Urbiet, B. Grandidier, S. G. Hickey, D. Vanmaekelbergh, *Phys. Rev. Lett.* **2006**, 97, 096803.
 [8] I. A. Zaluzhnyy, R. P. Kurta, A. André, O. Y. Gorobtsov, M. Rose, P. Skopintsev, I. Besedin, A. V. Zozulya, M. Sprung, F. Schreiber, I. A. Vartanyants, M. Scheele, *Nano Lett.* **2017**, 17, 3511.
 [9] J. J. Geuchies, C. van Overbeek, W. H. Evers, B. Goris, A. de Backer, A. P. Gantapara, F. T. Rabouw, J. Hilhorst, J. L. Peters, O. Konovalov, A. V. Petukhov, M. Dijkstra, L. D. A. Siebbeles, S. van Aert, S. Bals, D. Vanmaekelbergh, *Nat. Mater.* **2016**, 15, 1248.
 [10] K. Whitham, D.-M. Smilgies, T. Hanrath, *Chem. Mater.* **2018**, 30, 54.
 [11] M. C. Weidman, D.-M. Smilgies, W. A. Tisdale, *Nat. Mater.* **2016**, 15, 775.
 [12] J. Novák, R. Banerjee, A. Kornowski, M. Jankowski, A. André, H. Weller, F. Schreiber, M. Scheele, *ACS Appl. Mater. Interfaces* **2016**, 8, 22526.
 [13] T. Hanrath, J. J. Choi, D.-M. Smilgies, *ACS Nano* **2009**, 3, 2975.
 [14] D. V. Talapin, C. B. Murray, *Science* **2005**, 310, 86.
 [15] Y. Liu, M. Gibbs, J. Puthussery, S. Gaik, R. Ihly, H. W. Hillhouse, M. Law, *Nano Lett.* **2010**, 10, 1960.
 [16] S. J. Oh, N. E. Berry, J.-H. Choi, E. A. Gaulding, T. Paik, S.-H. Hong, C. B. Murray, C. R. Kagan, *ACS Nano* **2013**, 7, 2413.
 [17] W. H. Evers, J. M. Schins, M. Aerts, A. Kulkarni, P. Capiod, M. Berthe, B. Grandidier, C. Delerue, H. S. J. van der Zant, C. van Overbeek, J. L. Peters, D. Vanmaekelbergh, L. D. A. Siebbeles, *Nat. Commun.* **2015**, 6, 8195.
 [18] K. Whitham, J. Yang, B. H. Savitzky, L. F. Kourkoutis, F. Wise, T. Hanrath, *Nat. Mater.* **2016**, 15, 557.
 [19] D. M. Balazs, B. M. Matysiak, J. Momand, A. G. Shulga, M. Ibáñez, M. V. Kovalenko, B. J. Kooi, M. A. Loi, *Adv. Mater.* **2018**, 30, 1802265.
 [20] I. A. Zaluzhnyy, R. P. Kurta, M. Scheele, F. Schreiber, B. I. Ostrovskii, I. A. Vartanyants, *Materials* **2019**, 12, 3464.
 [21] N. Mukharamova, D. Lapkin, I. A. Zaluzhnyy, A. André, S. Lazarev, Y. Y. Kim, M. Sprung, R. P. Kurta, F. Schreiber, I. A. Vartanyants, M. Scheele, *Small* **2019**, 15, 1904954.
 [22] A. Dong, Y. Jiao, D. J. Milliron, *ACS Nano* **2013**, 7, 10978.
 [23] A. André, C. Theurer, J. Lauth, S. Maiti, M. Hodas, M. Samadi Khoshkhou, S. Kinge, A. J. Meixner, F. Schreiber, L. D. A. Siebbeles, K. Braun, M. Scheele, *Chem. Commun.* **2017**, 53, 1700.
 [24] S. Maiti, S. Maiti, A. Maier, J. Hagenlocher, A. Chumakov, F. Schreiber, M. Scheele, *J. Phys. Chem. C* **2019**, 123, 1519.
 [25] D. Qin, Y. Xia, G. M. Whitesides, *Nat. Protoc.* **2010**, 5, 491.
 [26] P. Nagpal, V. I. Klimov, *Nat. Commun.* **2011**, 2, 486.
 [27] Y. Zhang, D. Zherebetskyy, N. D. Bronstein, S. Barja, L. Lichtenstein, A. P. Alivisatos, L.-W. Wang, M. Salmeron, *ACS Nano* **2015**, 9, 10445.
 [28] M. C. Weidman, Q. Nguyen, D.-M. Smilgies, W. A. Tisdale, *Chem. Mater.* **2018**, 30, 807.
 [29] I. Lokteva, M. Koof, M. Walther, G. Grübel, F. Lehmkuhler, *Small* **2019**, 15, 1900438.
 [30] J. J. Choi, C. R. Bealing, K. Bian, K. J. Hughes, W. Zhang, D.-M. Smilgies, R. G. Hennig, J. R. Engstrom, T. Hanrath, *J. Am. Chem. Soc.* **2011**, 133, 3131.
 [31] S. Shaw, B. Yuan, X. Tian, K. J. Miller, B. M. Cote, J. L. Colaux, A. Migliori, M. G. Panthani, L. Cademartiri, *Adv. Mater.* **2016**, 28, 8892.
 [32] E. V. Shevchenko, D. V. Talapin, N. A. Kotov, S. O'Brien, C. B. Murray, *Nature* **2006**, 439, 55.
 [33] M. P. Boneschanscher, W. H. Evers, J. J. Geuchies, T. Altantzis, B. Goris, F. T. Rabouw, S. A. P. van Rossum, H. S. J. van der Zant, L. D. A. Siebbeles, G. van Tendeloo, I. Swart, J. Hilhorst, A. V. Petukhov, S. Bals, D. Vanmaekelbergh, *Science* **2014**, 344, 1377.
 [34] M. C. Weidman, M. E. Beck, R. S. Hoffman, F. Prins, W. A. Tisdale, *ACS Nano* **2014**, 8, 6363.
 [35] I. Moreels, K. Lambert, D. Smeets, D. de Muynck, T. Nollet, J. C. Martins, F. Vanhaecke, A. Vantomme, C. Delerue, G. Allan, Z. Hens, *ACS Nano* **2009**, 3, 3023.
 [36] S. Kalbfleisch, H. Neubauer, S. P. Krüger, M. Bartels, M. Osterhoff, D. D. Mai, K. Giewekemeyer, B. Hartmann, M. Sprung, T. Salditt, I. McNulty, C. Eyberger, B. Lai, *AIP Conf. Proc.* **2011**, 1365, 96.